

Transport evidence of Ising superconductivity in few-layer 1Td-MoTe₂

Jian Cui^{1,2†}, Peiling Li^{1,3†}, Jiadong Zhou^{4†}, Xiangwei Huang^{1,3}, Jian Yi⁵, Jie Fan¹, Zhongqing Ji¹, Xiunian Jing^{1,6}, Fanming Qu¹, Zhi Gang Cheng¹, Changli Yang^{1,6}, Li Lu^{1,6}, Kazu Suenaga⁷, Junhao Lin^{7*}, Zheng Liu^{4,8,9*} and Guangtong Liu^{1*}

¹Beijing National Laboratory of Condensed Matter Physics, Institute of Physics, Chinese Academy of Sciences, Beijing 100190, China

²Department of Physics, Liaoning University, Shenyang 110036, China

³University of Chinese Academy of Sciences, Beijing 100049, China

⁴Centre for Programmable Materials, School of Materials Science and Engineering, Nanyang Technological University, Singapore 639798, Singapore

⁵Ningbo Institute of Industrial Technology, Chinese Academy of Sciences, Ningbo 315201, China

⁶Collaborative Innovation Center of Quantum Matter, Beijing 100871, China

⁷National Institute of Advanced Industrial Science and Technology (AIST), Tsukuba 305-8565, Japan

⁸Centre for Micro-/Nano-electronics (NOVITAS), School of Electrical & Electronic Engineering, Nanyang Technological University, 50 Nanyang Avenue, Singapore 639798, Singapore

⁹CINTRA CNRS/NTU/THALES, UMI 3288, Research Techno Plaza, 50 Nanyang Drive, Border X Block, Level 6, Singapore 637553, Singapore

† These authors contributed equally to this work. Correspondence and requests for materials should be addressed to J.L. (email:lin.junhao@aist.go.jp), Z.L. (email: z.liu@ntu.edu.sg) and G.L. (email:gtliu@iphy.ac.cn)

Abstract

Unconventional superconductivity is one of the most fascinating and intriguing quantum phenomena in condensed matter physics. Recently, Ising superconductivity has been theoretically predicated and experimentally realized in noncentrosymmetric monolayer transition metal dichalcogenides (TMDCs) MX₂ (M =W, Mo and X=Te, Se, S). However, unconventional superconductivity in centrosymmetric TMDCs remains an open issue. Here, we report transport evidence of Ising superconductivity in few-layer 1Td-MoTe₂ crystals. Our low-temperature magnetotransport experiments show that the in-plane upper critical

field ($H_{c2,\parallel}$) is at least 6 times higher than the Pauli paramagnetic limit (H_p), which strongly suggests the Zeeman-protected Ising superconductivity in the sample. Our study sheds light on the interplay between unconventional superconductivity and crystal symmetry property, and may pave a new avenue to search for unconventional superconductors in centrosymmetric TMDCs.

Being an exotic quantum phenomenon, Ising superconductivity¹⁻³ has sparked intense research interest in condensed matter physics because it provides another ideal platform to engineer Majorana fermions⁴⁻⁸. Recent work has demonstrated Ising superconductivity in atomic-thin *noncentrosymmetric* 1H-phase transition metal dichalcogenides (TMDCs) such as few-layer NbSe₂¹ and MoS₂^{2,3}; due to the inversion symmetry breaking in 1H TMDCs, the spin-valley locking⁹ causes inequivalent valleys at corners of the hexagonal Brillouin zone, and leads to fascinating quantum phenomenon including Ising superconductivity¹⁻³, valley polarization^{10,11} and valley Hall effect¹². In this work, we provide transport data showing that Ising superconductivity can also be realized in *centrosymmetric* 1Td MoTe₂.

High crystalline few-layer MoTe₂ crystals were produced by molten-salt assisted chemical vapor deposition (CVD) method (see details in the *Materials and Methods* section and Figure S1). The crystal structure of 1T' MoTe₂ are shown in Figure 1a, and the optical images of as-synthesized MoTe₂ layers with different thicknesses are shown in Figure 1b. Similar to our previous results¹³, the mono- and few-layer MoTe₂ can have a size up to 100 μm with a rectangular shape. Figure 1c shows the Raman spectra of the as-synthesized MoTe₂ with different layers, where Ag modes of 1T' MoTe₂ were observed at 127, 161, 189 and 267 cm^{-1} , respectively, confirming the 1T' phase of our samples. Note that the Ag mode located at 267 cm^{-1} shows a blue-shift with increasing sample thickness, which is similar to the Raman shift in other two-dimensional (2D) materials such as MoS₂¹⁴ and WS₂¹⁵.

The atomic structure of few-layer MoTe_2 is further characterized by annular dark-field (ADF) scanning transmission electron microscopy imaging (STEM) and energy dispersive X-ray (EDX) spectrum. Figure 2a shows the STEM images of the monolayer region, where the upper is the experimental image and the lower is the simulation assuming $1T'$ phase crystallization (the right lower is the atomic model corresponding to the simulation). In the images, Te atoms are slightly brighter than Mo due to their larger atomic weight. The experimental image agrees well with the simulations, indicating that the film is crystallized in $1T'$ phase. Moreover, the fast Fourier transformation (FFT) pattern of the experimental image, as shown in the inset, manifests a rectangular unit cell and reveals the quasi-one-dimensional structure of the film, resulted from the rotational symmetry breaking by the distortion of Mo atoms and the formation of alternating Mo-Te chains as indicated in the atomic model.

Figure 2c shows the atom-resolved STEM image of few-layer MoTe_2 in large scale, with the chemical purity verified by EDX spectra where no signal of additional impurities is present (Figure 2b). As shown in Figure 2c, defects including vacancies and vacancy clusters readily show up in the few-layer region. These defects are due to oxidization by oxygen and water vapor of ambient atmosphere; they may give rise to an n-type doping¹⁶ and enhances the superconductivity in MoTe_2 , which will be discussed later. Also note that only small broken pieces of monolayer were observed in our samples, because monolayer films are more vulnerable to oxidization. By comparison with the simulated images shown in Fig. 2d, the experimental image indicates that at room temperature the stacking of the few-layer MoTe_2 is in the $1Td$ phase rather than the intrinsic $1T'$ phase ($1Td$ phase has a slight interlayer shift in the unit cell with respect to $1T'$). This is different from previous reports where the $1Td$ phase occurs at temperature

below 200 K^{16,17}. Presumably, this discrepancy may be attributed to the defect accumulation during the sample transfer process for STEM imaging.

Figure 3a shows the temperature dependence of the normalized four-terminal sheet resistance ($R/R_{300\text{K}}$), measured at zero magnetic field, for MoTe₂ films with thickness from 2 nm to 30 nm (See Supplementary Figure S1 for raw data). At high temperatures, all samples measured show a metallic behavior with $dR/dT > 0$, indicating that the phonon scattering dominates the transport. Then the samples enter a disorder-limited transport regime prior to the eventual superconducting state. The residual resistance ratio, $\text{RRR} = R_{300\text{K}}/R_{\text{N}}$ with $R_{300\text{K}}$ the room-temperature sheet resistance and R_{N} the normal-state sheet resistance right above the superconducting transition, varies from 1.15 of the 2.0-nm-thick to 2.33 of the 30-nm-thick MoTe₂ crystals (Supplementary Table 1). However, the largest sheet resistance $R_{\text{N}} = R_{5\text{K}} = 810 \text{ } \Omega/\text{sq}$ found in the 2.0-nm-thick device is much smaller than the quantum resistance $R_{\text{Q}} = h/(2e)^2 = 6,450 \text{ } \Omega$ ¹⁸, suggesting that our samples are all in the low-disorder regime.

At low temperatures, superconductivity is observed for all samples, and to examine closely the thickness-dependent superconductivity, in Fig. 3b we show the temperature dependence of the reduced resistance, $r = R/R_{\text{N}} = R/R_{5\text{K}}$, in a low-temperature regime $T \leq 5.5 \text{ K}$ for samples of different thickness. Empirically, critical transition temperatures for the superconductivity, $T_{\text{c},r}$, can be extracted from the r vs T curve, by searching from the normal state into the superconducting state and picking up the points firstly encountered with the predefined reduced resistance r . Such transition temperatures, extracted at typical values $r=0, 0.5$, and 0.9 , are listed in supplementary Table S1 for our samples with different thickness. It is found that, $T_{\text{c},0}$ increase from 0.35 K to 3.16 K with increasing sample thickness from 2 nm to 30 nm, and the

$T_{c,0}$ values of our samples are surprisingly higher than $T_{c,0} \sim 0.1$ K as reported in stoichiometric bulk MoTe₂¹⁷. In bulk MoTe₂, Te-vacancy-enhanced superconductivity has been previously reported¹⁶ with the highest $T_{c,0} \sim 1.3$ K that is, however, much lower than $T_{c,0} = 3.16$ K observed in our 30-nm-MoTe₂ crystals. The superconductivity enhancement observed in our samples may be accounted for by the n-type doping induced by the defects, revealed by the STEM measurements shown in Fig. 2c, though the underlying mechanism is still unclear and needs further study. In addition, a significant broadening on superconducting transition are observed for 2-nm-thick device, which can be attributed to enhanced thermal fluctuations in two dimensions^{19,20}; similar behaviors have been observed in few-layer Mo₂C²¹ and NbSe₂^{1,22} superconductors reported recently.

The few-layer MoTe₂ crystals provide an ideal platform to study the transport properties in the 2D limit. To investigate the dimensionality of the superconductivity in few-layer MoTe₂, at first we studied the temperature dependence of the upper critical magnetic field $\mu_0 H_{c2}$ defined as the magnetic field corresponding to a predefined reduced resistance $r = R/R_N$. Figure 4a,b show the superconducting resistive transitions of a 8.6-nm-thick MoTe₂ device with the magnetic field perpendicular and parallel to the sample surface, respectively, measured at fixed temperatures. In both cases, one can see that the superconducting transition shifts gradually to lower magnetic fields with the increase of temperature; the temperature-dependent upper critical fields in directions parallel and perpendicular to the sample surface, denoted by $\mu_0 H_{c2,\parallel}$ and $\mu_0 H_{c2,\perp}$ respectively, are plotted in Figure 4c for the case of $r = 0.9$. We found that the superconductivity was more susceptible to perpendicular magnetic fields than to parallel magnetic fields, and a large ratio of $H_{c2,\parallel}/H_{c2,\perp} \approx 7$ is obtained in the 8.6-nm-thick sample, indicating a strong magnetic anisotropy. This is true for all samples, and the ratio reaches up to

23 for 2.7-nm-thick sample (see Supplementary Fig. S3 for more data on other samples). A linear temperature dependence was observed for $H_{c2,\perp}$, which can be well fitted by the phenomenological 2D Ginzburg-Landau (GL) theory¹⁹,

$$H_{c2,\perp}(T) = \frac{\phi_0}{2\pi\xi_{GL}^2} \left(1 - \frac{T}{T_{c,0}}\right), \quad (1)$$

where ξ_{GL} is the zero-temperature GL in-plane coherence length and ϕ_0 is the magnetic flux quantum, as shown by blue dashed line in Fig. 4c that gives $\xi_{GL} = 19.7$ nm (See Supplementary Table S1 and Fig. S3 for more data). The $H_{c2,\parallel}(T)$, saturating at low temperature, has temperature dependence that can also be well fitted by the 2D GL model¹⁹,

$$H_{c2,\parallel}(T) = \frac{\phi_0\sqrt{12}}{2\pi\xi_{GL}d_{sc}} \sqrt{1 - \frac{T}{T_{c,0}}}, \quad (2)$$

where d_{sc} is the superconducting thickness, as shown by the red curve in Fig. 4c that gives $d_{sc} = 8.2$ nm. The $d_{sc} = 8.2$ nm obtained from the fitting is consistent with the sample thickness of 8.6 nm as measured by AFM (Supplementary Fig. S3f), and the coherence length from the fitting $\xi_{GL} = 19.7$ nm is two times of the thickness. In addition to the excellent fittings by the 2D model, these strongly suggest the 2D nature of the superconductivity in this few-layer MoTe₂ crystal (See Supplementary Table S1 for similar data on other samples with different thickness).

The dimensionality of a given superconductor can also be evaluated by the experiments with tilted magnetic field. Figure 4d shows the magnetic field dependence of the sheet resistance R under different θ at 0.3 K, where θ is the tilted angle between the normal of the sample plane and the direction of the applied magnetic field, as shown in the inset of Fig. 4c. As shown in Fig. 4d, the superconducting transition shifts to higher field with the external magnetic field rotating from

perpendicular $\theta=0^\circ$ to parallel $\theta=90^\circ$ (See Supplementary Fig. S4 for more data on different MoTe₂ samples). The upper critical field $\mu_0 H_{c2}$, also defined as the magnetic field where $r = 0.9$, was extracted from Fig. 4d and plotted in Figure 4e against the tilted angle θ . In Fig. 4e, a cusp-like peak is clearly observed at $\theta=90^\circ$ where the external magnetic field is aligned in parallel to the sample surface, which is apparently sharper for thinner sample (Supplementary Fig. S4). The cusp can be fitted with the 2D Tinkham model¹⁹ and 3D anisotropic mass model (3D-GL), respectively. As shown in the inset of Fig. 4e, we found that the data can be much better fitted by the former model, manifesting the 2D nature of the superconductivity.

Moreover, for a 2D superconductor with $d_{sc} \ll \xi_{GL}$, the superconducting phase transition is expected to follow the Berezinskii-Kosterlitz-Thouless (BKT) theory. According to the theory, there are bound vortex-antivortex pairs in the superconducting phase at low temperature. If a heating current is applied to the superconductor, these pairs will split and move freely, leading to a nonlinear voltage dependence: $V \propto I^{\alpha(T)}$. The characteristic temperature T_{BKT} defines the vortex unbinding transition and can be determined by measuring $V-I$ curves as a function of temperatures, as shown in Fig. 5a on a log-log scale for data taken from a 3-nm thick sample. At T_{BKT} , a 2D superconductor obeys the universal scaling relation $V \propto I^3$ denoted by the blue solid line in Fig. 5a. Figure 5b shows the temperature dependence of exponent α , which is extracted from the slope of $V-I$ traces shown in Fig. 5a. From Fig. 5b, the BKT transition temperature corresponding to $\alpha=3$ is estimated to be $T_{BKT}=1.47$ K, only slightly larger than $T_{c,0}=1.4$ K of the sample. The consistency of the BKT transition can be additionally checked by analyzing the temperature-dependent resistance at zero magnetic field. At temperatures just above T_{BKT} , R is expected to follow the relation

$$R(t) = R_0 \exp(-bt^{-1/2}), \quad (3)$$

where R_0 and b are material-specific parameters, and $t = T/T_{BKT} - 1$ is the reduced temperature. As shown in Fig. 5c, the temperature-dependent resistance can be well fitted with the above formula Eq. (3). The best fitting gives $T_{BKT}=1.4$ K, in good agreement with the nonlinear $V-I$ measurement. The observation on BKT transition further attests the 2D nature of the superconductivity in these few-layer MoTe_2 samples.

With above evidences, we believe that the 2D superconductivity is convincingly confirmed in our few-layer 1Td MoTe_2 samples. Now we turn to discuss the other remarkable finding of our experiments, i.e., the observation of anomalous enhancement of the in-plane upper critical field $H_{c2,\parallel}$.

For conventional Bardeen-Cooper-Schrieffer (BCS) superconductors, sufficiently high external magnetic field can destroy the superconductivity by breaking Cooper pairs via the coexisting orbital^{19,23} and Zeeman spin splitting effect^{24,25}. The orbital contribution originates from the coupling between the external magnetic field and the electron momentum, whereas the Zeeman spin splitting contribution comes from spin alignment within Cooper pairs by the external magnetic field. For the few-layer sample, the orbital effect of the in-plane magnetic field is greatly suppressed due to the reduced dimensionality¹⁹, and consequently $H_{c2,\parallel}$ is solely determined by the interaction between the external magnetic field and the spin of Cooper pairs. When the Zeeman spin splitting energy from the applied magnetic field approaches the superconducting energy gap, the Cooper pairs are broken and superconductivity is destroyed at a characteristic field given by the Clogston-Chandrasekhar²⁵ or Pauli paramagnetic limit $H_p = \sqrt{2}\Delta_0/(g\mu_B)$, where $\Delta_0=1.76k_B T_c$, g the g factor and μ_B the Bohr magneton. Therefore, for

BCS superconductors with weak orbital coupling, the upper critical field H_{c2} should be smaller than the usual Pauli limit $H_p = 1.86T_c(0)$. However, the values of H_{c2} shown in Fig. 4f for the five typical samples with different thicknesses are all larger than H_p , in marked contrast to their bulk counterpart that is well below the H_p ¹⁷. Interestingly, $H_{c2,\parallel}/H_p$ shows a linear dependence on sample thickness d . For the 2.7-nm-thick (2 or 3 layers) MoTe₂ device, the ratio of $H_{c2,\parallel}/H_p$ attains 6.3, which already exceeds the largest value of $H_{c2,\parallel}/H_p \approx 5$ observed in monolayer NbSe₂¹ and ion-gated MoS₂³. This unusual enhancement of $H_{c2,\parallel}$ strongly suggests that the superconductivity in few-layer MoTe₂ is unconventional.

Similar anomalous enhancement of $H_{c2,\parallel}$ has been observed in layered superconductors in the dirty limit with strong spin-orbital coupling (SOC), which can be explained by spin-orbit scattering²⁶⁻³¹ (SOS) effect using the microscopic Klemm-Luther-Beasley (LKB) theory³⁰. However, the SOS mechanism is inadequate to interpret our data because the samples are in the low-disorder regime as discussed earlier. It is known that inhomogeneous superconducting states, such as Fulde-Ferrell-Larkin-Ovchinnikov (FFLO) state³²⁻³⁵ or helical state³⁶, can also enhance $H_{c2,\parallel}$, which have been observed in heavy Fermion superconductors³², organic superconductors^{37,38}, and monolayer Pb films³⁹. However, for superconductors induced by FFLO state, the theoretical value³⁷ of $H_{c2,\parallel}/H_p$ is in the range of 1.5~2.5, much smaller than the observed value of 6.3 in our 2.7-nm-thick sample; therefore the FFLO state can be safely ruled out. Similarly, we can exclude the mechanism of Rashba SOC in non-centrosymmetric superconductors, which can only enhance $H_{c2,\parallel}$ up to $\sqrt{2}H_p$ at most⁴⁰.

In monolayer NbSe₂ and gated MoS₂ superconductor, the anomalous enhancement of $H_{c2,\parallel}$ has been interpreted by the Zeeman-protected Ising superconductivity mechanism¹⁻³. The monolayer

TMDCs with 1H structure possess out-of-plane mirror symmetry and in-plane inversion symmetry breaking simultaneously. The mirror symmetry restricts the crystal field (ϵ) to the plane, while the inversion symmetry breaking can induce strong SOC, giving rise to an effective Zeeman-like magnetic field $H_{so}(\mathbf{k}) \propto \mathbf{k} \times \epsilon$ (~ 100 T for gated MoS_2 and ~ 660 T for NbSe_2) with opposite out-of-plane direction at the K and $-\text{K}$ valleys of the Brillouin zone⁴¹. Thus the electron spin is aligned along the out-of-plane direction, and they are antiparallel to each other for electrons with opposite momenta; therefore, spins of electrons in Cooper pairs are polarized by the large out-of-plane Zeeman field, which protects them from being realigned by an external in-plane magnetic field and leads to an enhancement of in-plane $H_{c2,\parallel}$. This mechanism of superconductivity in non-centrosymmetric monolayer TMDCs, referred to as Ising superconductivity, will be suppressed in the 3D bulk due to destruction of the spin-valley locking when the inversion symmetry and spin degeneracy are restored.

Our data displayed in Fig. 4f show that $H_{c2,\parallel}/H_p$ increases dramatically as the sample becomes thinner, also strongly suggesting Ising superconducting mechanism that is sensitive to the sample thickness. Presumably, the crystalline structure of MoTe_2 is centrosymmetric and there should be no out-of-plane spin polarization due to an effective magnetic field, and spin-resolved laser ARPES⁴² measurements have indeed confirmed that bulk MoTe_2 has only an in-plane spin-polarization. Hence the observation of Ising superconductivity in our few-layer MoTe_2 samples remains puzzling, though it is possible that somehow the SOC can be strong in thin few-layer MoTe_2 and give rise to Ising superconductivity⁴³. Compared to the extensively studied Ising superconductivity in 2H phase (noncentrosymmetric) TMDCs^{1-3,44,45}, there is no experimental and theoretical studies of Ising superconductivity in centrosymmetric (1Td phase) TMDCs before this work. It is interesting for physicists to see whether symmetry breaking is a necessary

condition for Ising superconductivity. For material scientists, it may open up a new way to search for unconventional superconductors in centrosymmetric TMDCs.

In summary, for the first time, intrinsic 2D superconductivity on highly crystalline atomic-thin MoTe₂ films, synthesized via CVD method, is demonstrated by low-temperature transport measurements. Remarkable anomalous enhancement of the in-plane upper critical field $H_{c2,\parallel}$ is observed and strongly suggests Ising pairing for the mechanism of superconductivity. Our findings indicate that highly crystalline monolayer TMDCs can provide a new material platform to study 2D topological superconductivity, helping to deepen our understanding of the topological state and pave a way for the applications of quantum devices.

Materials and Methods

CVD synthesis of highly crystalline few-layer MoTe₂. The few-layer MoTe₂ samples were synthesized via CVD method inside a furnace with a 1 inch diameter quartz tube. Specifically, one alumina boat containing precursor powder (NaCl: MoO₃=1:5) was put in the center of the tube. Si substrate with a 285 nm thick SiO₂ on top was placed on the alumina boat with polished side faced down. Another alumina boat containing Te powder was put on the upstream side of quartz tube at a temperature of about 450 °C. Mixed gas of H₂/Ar with a flow rate of 15/80 sccm was used as the carrier gas. The furnace was ramped to 700 °C at a rate of 50 °C/min and held there for about 4 min to allow the growth of few-layer MoTe₂ crystals. After the reaction, the temperature was naturally cooled down to room temperature. All reagents were purchased from Alfa Aesar with purity exceeding 99%.

Raman Characterization. Raman measurements with an excitation laser of 532 nm were performed using a WITEC alpha 300R Confocal Raman system. Before the characterization, the

system was calibrated with the Raman peak of Si at 520 cm^{-1} . The laser power is less than 1 mW to avoid overheating of the samples.

TEM and STEM Characterization. The STEM samples were prepared with a poly (methyl methacrylate) (PMMA) assisted method. A layer of PMMA of about $1\text{ }\mu\text{m}$ thick was firstly spin-coated on the wafer with MoTe_2 samples deposited, and then baked at $180\text{ }^\circ\text{C}$ for 3min. The wafer was then immersed in NaOH solution (1M) overnight to etch the SiO_2 layer. After lift-off, the PMMA/ MoTe_2 film was transferred into distilled (DI) water for several cycles to rinse off the residual contaminants, and then it was fished by a TEM grid (Quantifoil Au grid). The transferred specimen was dried naturally in ambient environment, and then dropped into acetone overnight to dissolve the PMMA coating layers. The STEM imaging on MoTe_2 were performed on a JEOL 2100F with a cold field-emission gun and a DELTA aberration corrector operating at 60 kV. A Gatan GIF Quantum was used to record the EELS spectra. The inner and outer collection angles for the STEM images (β_1 and β_2) were 62 and 129–140 mrad, respectively, with a convergence semi-angle of 35 mrad. The beam current was about 15 pA for the ADF imaging and EELS chemical analyses. All imaging was performed at room temperature.

Devices fabrication and transport measurement. Few-layer MoTe_2 crystals with the thickness ranging from 2 nm to 30 nm were firstly identified by their color contrast under optical microscopy. Then small markers were fabricated using standard e-beam lithography (EBL) near the identified sample for subsequent fabrication of Hall-bar devices. To obtain a clean interface between the electrodes and the sample, *in situ* argon plasma was employed to remove the resist residues before metal evaporation without breaking the vacuum. The Ti/Au (5/70 nm) electrodes were deposited using an electron-beam evaporator followed by lift-off in acetone. Transport experiments were carried out with a standard four-terminal method from room temperature to 0.3

K in a top-loading Helium-3 refrigerator with a 15 T superconducting magnet. A standard low-frequency lock-in technique was used to measure the resistance with an excitation current of 10 nA. Angular-dependent measurements were facilitated by an *in situ* home-made sample rotator.

Acknowledgements

The authors thank Xianxin Wu, Heng Fan, Jianlin Luo, Hsin Lin, and Jiangping Hu for stimulating discussions. This work has been supported by the National Basic Research Program of China from the MOST under the grant No. 2014CB920904, 2015CB921101 and 2016YFA0300600, by the NSFC under the grant Nos. 11527806 and 11174340. Research in Singapore was funded by National Research Foundation under NRF RF Award No. NRF-RF2013-08, the start-up funding from Nanyang Technological University (M4081137.070). J.L. and K.S. acknowledge JST-ACCEL and JSPS KAKENHI (JP16H06333 and P16382) for financial support.

Author contributions

J.C., P.L. and J.Z. contributed equally to this work. G.L. and Z.L. conceived and supervised the project, and designed the experiments; J.C., P.L. and X.H. fabricated the devices and carried out the transport measurements under the supervision of G.L.; J.Z. carried out the sample growth experiments under the supervision of Z.L.; J.L. did the measurements and data analysis on STEM; G.L. and Z.L. prepared the manuscript with input from J.L. and J.Z. All the authors discussed the results and commented on the manuscript.

Additional information

Supplementary information is available in the online version of the paper. Reprints and permissions information is available online at www.nature.com/reprints.

Correspondence and requests for materials should be addressed to G.L, Z.L. or J.L.

Competing financial interests

The authors declare no competing financial interests.

Figure and Figure Caption

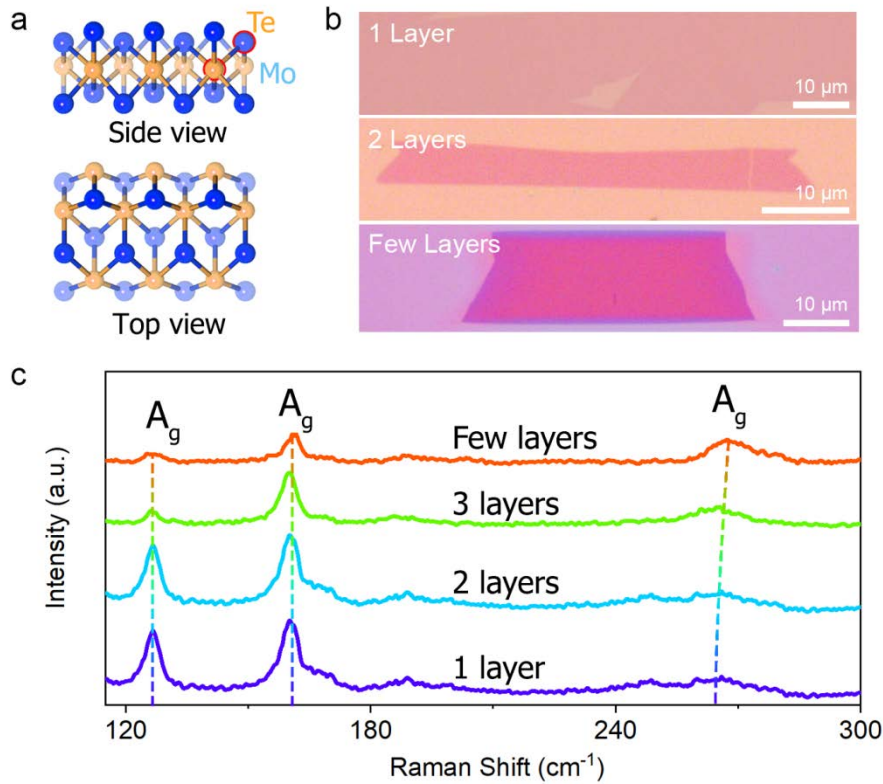


Figure 1 | Optical images and Raman spectra of the as-synthesized MoTe₂ layers. **a**, Side and top views of the crystal structure of 1T'-MoTe₂, respectively. **b**, Optical images of monolayer (1L), bilayer (2L) and few layers of as-produced MoTe₂. The size of the monolayer sample can reach up to 100 μm. **c**, Raman spectra of few-layer MoTe₂ samples. Raman peaks were observed at 127, 161, 189 and 267 cm⁻¹, corresponding to the Ag modes of 1T'-MoTe₂.

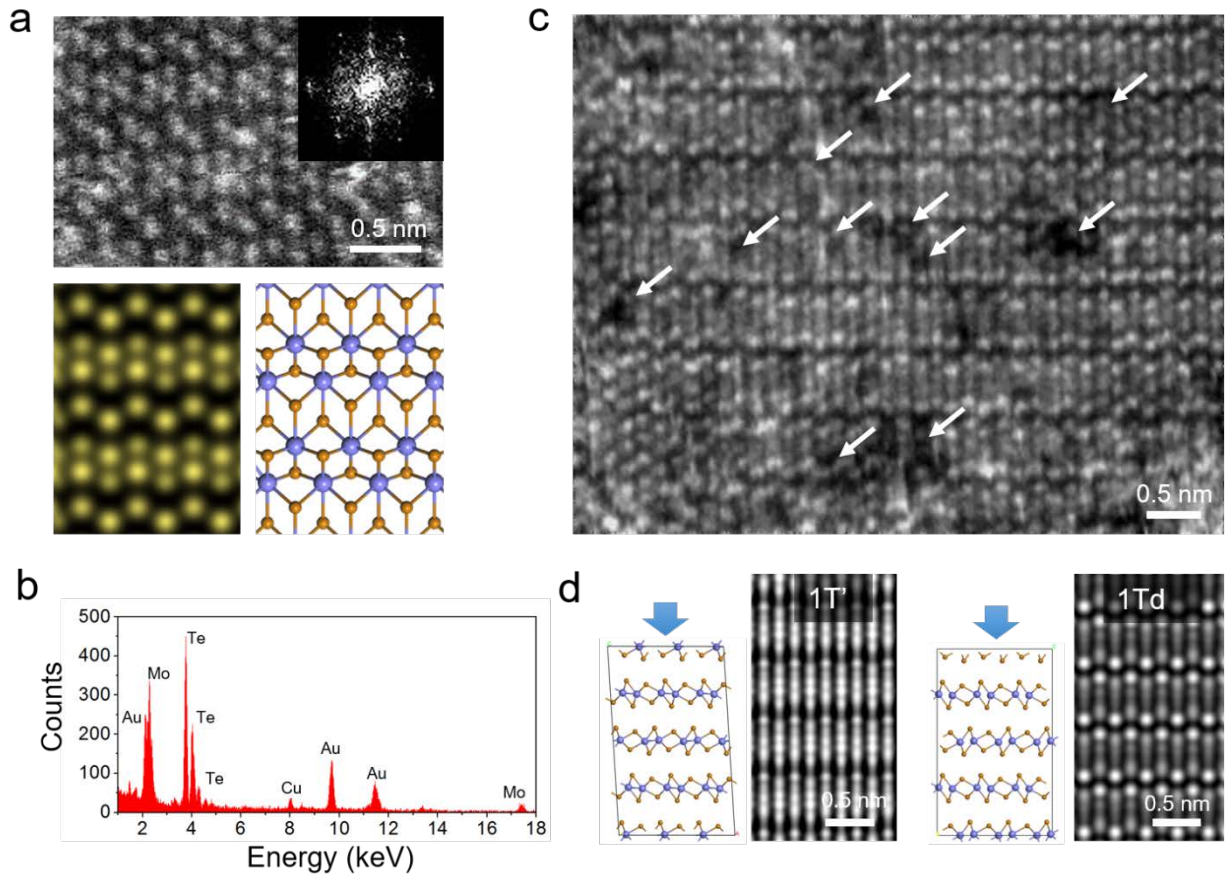


Figure 2 | ADF-STEM images, and EDX characterizations of the as-synthesized MoTe₂ crystals. **a**, Atomic resolution ADF-STEM image of the MoTe₂ monolayer region. Inset: FFT pattern of the image. The simulated STEM image and the atomic model of monolayer MoTe₂ are shown below the experimental image. **b**, Energy-dispersive X-ray spectrometry (EDX) spectrum of the few-layer MoTe₂. The Au and Cu signal comes from the reflection of TEM grid bar and the pole piece. **c**, Atomic resolution STEM image of few-layer MoTe₂. The arrows indicate the sites of vacancies or vacancy clusters. **d**, Simulated STEM images of few-layer MoTe₂ viewed along [001] with 1T' and 1Td stacking, respectively.

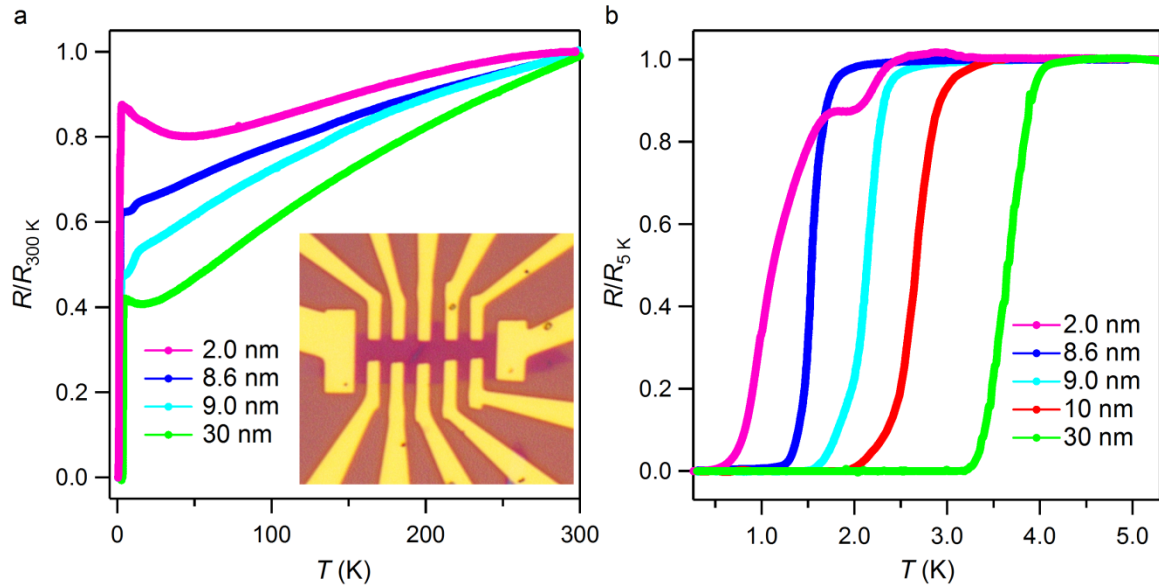


Figure 3 | Thickness dependence of the superconductivity in MoTe₂. **a**, Temperature dependence of the normalized four-terminal resistance ($R/R_{300\text{K}}$) for MoTe₂ devices with thicknesses ranging from 2.0 nm to 30 nm. The inset is a typical Hall-bar device used for the measurements. **b**, Temperature dependence of the reduced four-terminal resistance, $r = R/R_{5\text{K}}$ in the range from 0.3 K to 5.5 K, for MoTe₂ devices with various thicknesses from 2.0 nm to 30 nm..

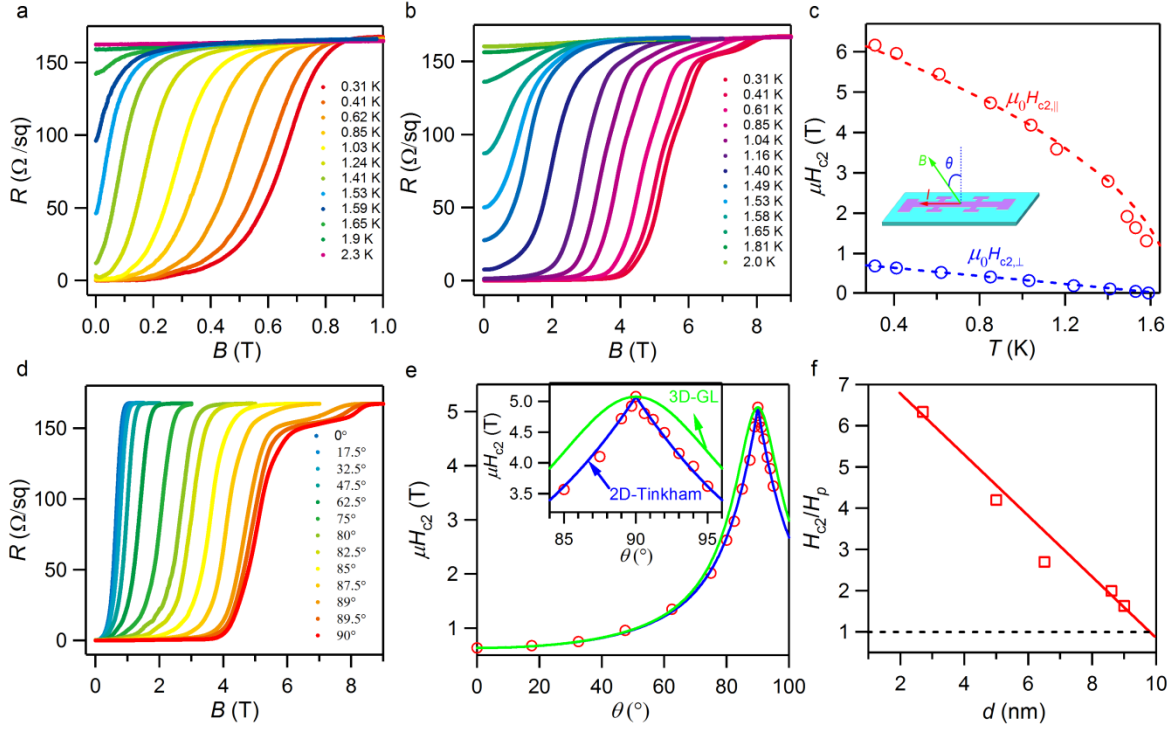


Figure 4 | Two-dimensional superconductivity of few-layer MoTe₂ crystals. **a, b,**

Superconducting resistive transition of the 8.6-nm-thick MoTe₂ crystal in perpendicular magnetic field **(a)** and in parallel magnetic field **(b)**. **c,** Temperature dependence of the upper

critical field $\mu_0 H_{c2}$ corresponding to reduced resistance $r = 0.9$, with magnetic field directions parallel ($\mu_0 H_{c2,\parallel}$) and perpendicular ($\mu_0 H_{c2,\perp}$) to the crystal plane. Dashed curves are fittings to the 2D Ginzburg-Landau theory. The inset is a schematic drawing of the tilt experiment setup. **d,**

Magnetic field dependence of the sheet resistance of the 8.6-nm MoTe₂ device at $T=0.3$ K with different tilted angles θ (θ is the angle between a magnetic field and the normal of the sample plane). **e,** Angular dependence of the upper critical field $\mu_0 H_{c2}$. The inset shows a zoom-in view

of the region around $\theta=90^\circ$. The solid lines represent the fitting with the 2D Tinkham formula

$$\left| \frac{H_{c2}(\theta) \cos \theta}{H_{c2,\perp}} \right| + \left(\frac{H_{c2}(\theta) \sin \theta}{H_{c2,\parallel}} \right)^2 = 1 \text{ (blue line) and the 3D anisotropic mass model (3D-GL)}$$

$$\left(\frac{H_{c2}(\theta) \cos \theta}{H_{c2,\perp}}\right)^2 + \left(\frac{H_{c2}(\theta) \sin \theta}{H_{c2,\parallel}}\right)^2 = 1 \text{ (green line), respectively. } \mathbf{f}, \text{ Normalized upper critical field}$$

H_{c2}/H_p as a function of sample thickness d . The red solid line is a guide to the eye and the dashed line denotes the Pauli limit $H_{c2}=H_p$.

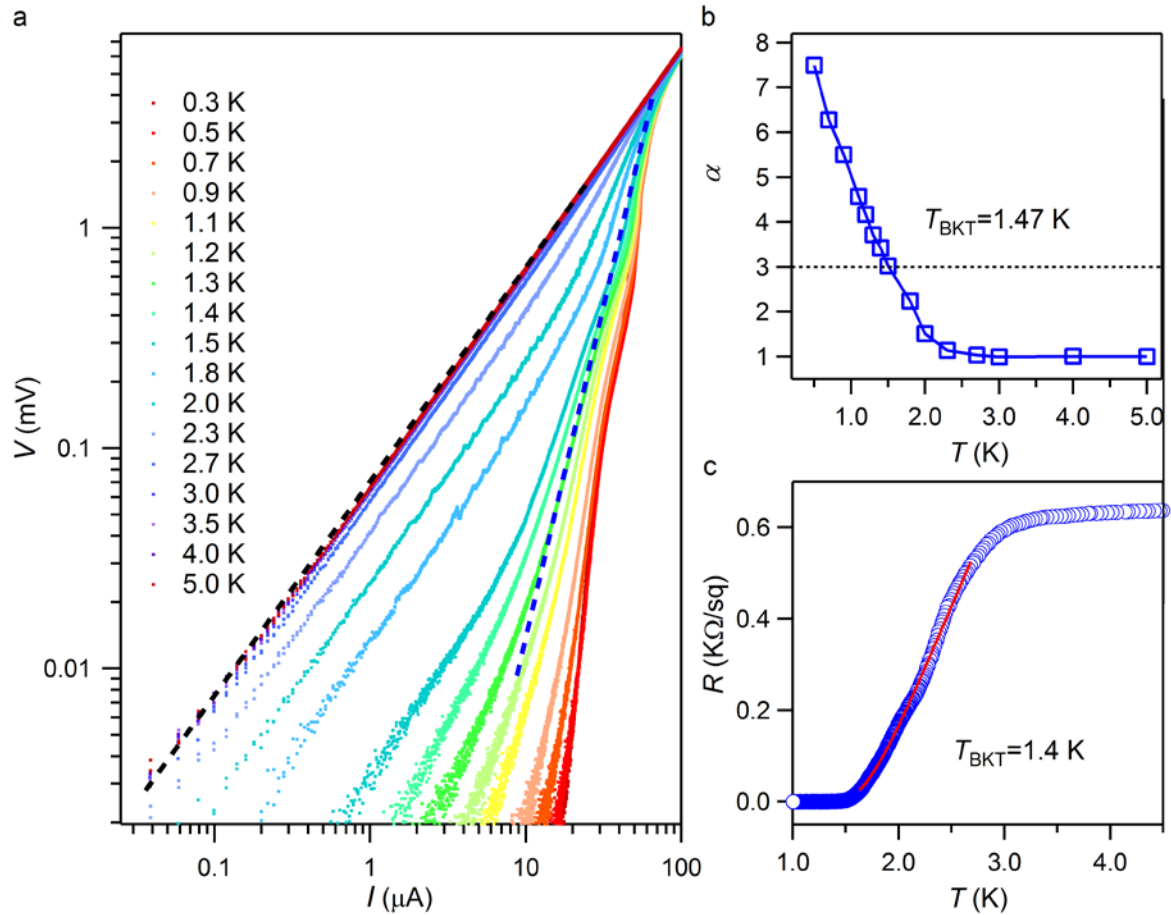


Figure 5 | BKT transition in the 3-nm-thick MoTe₂ crystal. **a**, Voltage-current behavior (V - I) at different temperatures close to T_c plotted on a logarithmic scale. The black dashed line indicates the ohmic behavior expected in the normal state. The blue dashed line indicates $V \propto I^3$, which corresponds to $T = T_{\text{BKT}}$. **b**, Temperature dependence of the exponent α obtained from fittings data in (a) to $V \propto I^\alpha$. $T_{\text{BKT}} = 1.47 \text{ K}$ is obtained from the intersection between the experimental curve and the dashed black line $\alpha = 3$. **c**, Temperature dependence of the zero-field resistance. The red line is a fit to the expected BKT transition, yielding $T_{\text{BKT}} = 1.4 \text{ K}$.

Reference:

1. Xi, X. X. *et al.* Ising pairing in superconducting NbSe₂ atomic layers. *Nat Phys.* **9**, 139-143 (2016).
2. Saito, Y. *et al.* Superconductivity protected by spin–valley locking in ion-gated MoS₂. *Nat Phys.* **12**, 144-150 (2016).
3. Lu, J. M. *et al.* Evidence for two dimensional Ising superconductivity in gated MoS₂. *Science* **350**, 1353-1357 (2015).
4. Zhou, B. T. *et al.* Ising superconductivity and Majorana fermions in transition-metal dichalcogenides. *Phys. Rev. B* **93**, 180501(R) (2016).
5. Sharma, G. and Tewari, S. Yu-Shiba-Rusinov states and topological superconductivity in Ising paired superconductors. *Phys. Rev. B* **94**, 094515 (2016).
6. Hsu, Y.-T. *et al.* Topological superconductivity in monolayer transition metal dichalcogenides. *Nat. Commun.* **8**, 14985 (2016).
7. Zhang, J. and Aji, V. Topological Yu-Shiba-Rusinov chain in monolayer transition-metal dichalcogenide superconductors. *Phys. Rev. B* **94**, 060501 (2016).
8. He, W. Y. *et al.* Nodal topological superconductivity in monolayer NbSe₂. *arXiv*: 1604.02867.
9. Xu, X. D. *et al.* Spin and pseudospins in layered transition metal dichalcogenides. *Nat. Phys.* **10**, 343-350 (2014).
10. Zeng, H. *et al.* Valley polarization in MoS₂ monolayers by optical pumping. *Nature Nanotech.* **7**, 490-493 (2012).
11. Mak, K. F. *et al.* Control of valley polarization in monolayer MoS₂ by optical helicity. *Nat. Nanotechnol.* **7**, 494 (2012).
12. Mak, K. F. *et al.* The valley Hall effect in MoS₂ transistor. *Science.* **344**, 1489-1492 (2014).
13. Zhou, J. D. *et al.* Large-area and high-quality 2D transition metal telluride. *Adv. Mat.* **29**, 1603471 (2017).
14. Li, H. *et al.* From Bulk to Monolayer MoS₂: Evolution of Raman Scattering. *Adv. Funct. Mater.* **22**, 1385-1390 (2012).
15. Berkdemir, A. *et al.* Identification of individual and few layers of WS₂ using Raman Spectroscopy. *Sci. Rep.* **3**, 1755 (2013).
16. Cho, S. *et al.* Te vacancy-driven superconductivity in orthorhombic molybdenum ditelluride. *2D Mater.* **4**, 021030 (2017).
17. Qi, Y. P. *et al.* Superconductivity in Weyl semimetal candidate MoTe₂. *Nat. Commun.* **7**, 11038 (2015).
18. Fiory, A. T. and Hebard, A. F. Electron mobility, conductivity, and superconductivity near the metal-insulator transition. *Phys. Rev. Lett.* **52**, 2057-2060 (1984).

19. Tinkham, M. *Introduction to Superconductivity* 2nd edn (McGraw-Hill, 1996).
20. Beasley, M. R. *et al.* Possibility of vortex-antivortex pair dissociation in two-dimensional superconductors. *Phys. Rev. Lett.* **42**, 1165-1168 (1979).
21. Xu, C. *et al.* Large-area high-quality 2D ultrathin Mo₂C superconducting crystals. *Nat. Mater.* **14**, 1135-1141 (2015).
22. Wang, H. *et al.* High-quality monolayer superconductor NbSe₂ grown by chemical vapour deposition. *Nat. Commun.* **8**, 394 (2017).
23. Hess, H. F. *et al.* Scanning-tunneling-microscope observation of the Abrikosov flux lattice and the density of states near and inside a fluxoid. *Phys. Rev. Lett.* **62**, 214-216 (1989).
24. Chandrasekhar, B. S. A note on the maximum critical field of high-field superconductors. *Appl. Phys. Lett.* **1**, 7-8 (1962).
25. Clogston, A. M. Upper limit for critical field in hard superconductors. *Phys. Rev. Lett.* **9**, 266-267 (1962).
26. Prober, D. E. *et al.* Upper critical fields and reduced dimensionality of the superconducting layered compounds. *Phys. Rev. B* **21**, 2717-2733 (1980).
27. Tedrow, P. M. *et al.* Critical magnetic field of very thin superconducting aluminum films. *Phys. Rev. B* **25**, 171-178 (1982).
28. Maki, K. Effect of Pauli paramagnetism on magnetic properties of high-field superconductors. *Phys. Rev.* **148**, 362-369 (1966).
29. Werthamer, N. R. *et al.* Temperature and purity dependence of superconducting critical field, H_{c2}. III. Electron spin and spin-orbit effects. *Phys. Rev.* **147**, 295-302 (1966).
30. Klemm, R. A. *et al.* Theory of upper critical field in layered superconductors. *Phys. Rev. B* **12**, 877-891 (1975).
31. Meservey, R. & Tedrow, P. M. Spin-orbit scattering in superconducting thin films. *Phys. Lett. A* **58**, 131-132 (1976).
32. Matsuda, Y. *et al.* Fulde-Ferrell-Larkin-Ovchinnikov state in heavy fermion superconductors. *J. Phys. Soc. Jpn.* **76**, 051005 (2007).
33. Fulde, P.; Ferrell, R. A. Superconductivity in a strong spin-exchange field. *Phys. Rev.* **135**, A550-A563 (1964).
34. Larkin, A. I. & Ovchinnikov, Y. N. Nonuniform state of superconductors. *Sov. Phys. JETP* **20**, 762-769 (1965).
35. Liu, C. X. Unconventional Superconductivity in Bilayer Transition Metal Dichalcogenides. *Phys. Rev. Lett.* **118**, 087001 (2017).
36. Kaur, R. P. *et al.* Helical vortex phase in the noncentrosymmetric CePt₃Si. *Phys. Rev. Lett.* **94**, 137002 (2005).

37. Agosta, C. C. *et al.* Experimental and semiempirical method to determine the Pauli-limiting field in quasi-two-dimensional superconductors as applied to κ -(BEDT-TTF)₂Cu(NCS)₂: Strong evidence of a FFLO state. *Phys. Rev. B* **85**, 214514 (2012).
38. Shimahara, H. Fulde-Ferrell-Larkin-Ovchinnikov State in a quasi-two-dimensional organic superconductor. *J. Phys. Soc.* **66**, 541-544 (1997).
39. Sekihara, T. *et al.* Two dimensional superconducting state of monolayer Pb films grown on GaAs(110) in a strong parallel magnetic field. *Phys. Rev. Lett.* **111**, 057005 (2013).
40. Gorkov, L. P. and Rashba, E. I. Superconducting 2D system with lifted spin degeneracy: mixed singlet-triplet State. *Phys. Rev. Lett.* **87**, 037004 (2001).
41. Kormányos, A. *et al.* Monolayer MoS₂: Trigonal warping, the Γ valley, and spin-orbit coupling effects. *Phys. Rev. B* **88**, 045416 (2013).
42. Sakano, M. *et al.* Observation of spin-polarized bands and domain-dependent Fermi arcs in polar Weyl semimetal MoTe₂. *Phys. Rev. B* **95**, 421101(R) (2017).
43. Liu, J. W. and Law, K. T. *et al.* private communication.

Supplementary Information

Ising superconductivity in highly crystalline few-layer 1T'-MoTe₂

Jian Cui^{1,2†}, Peiling Li^{1,3†}, Jiadong Zhou^{4†}, Xiangwei Huang^{1,3}, Jian Yi⁵, Jie Fan¹, Zhongqing Ji¹, Xiunian Jing^{1,6}, Fanming Qu¹, Zhi Gang Cheng¹, Changli Yang^{1,6}, Li Lu^{1,6}, Kazu Suenaga⁷, Junhao Lin^{7*}, Zheng Liu^{4,8,9*} and Guangtong Liu^{1*}

¹Beijing National Laboratory for Condensed Matter Physics, Institute of Physics, Chinese Academy of Sciences, Beijing 100190, China

²Department of Physics, Liaoning University, Shenyang 110036, China

³University of Chinese Academy of Sciences, Beijing 100049, China

⁴Centre for Programmable Materials, School of Materials Science and Engineering, Nanyang Technological University, Singapore 639798, Singapore

⁵Ningbo Institute of Industrial Technology, Chinese Academy of Sciences, Ningbo 315201, China

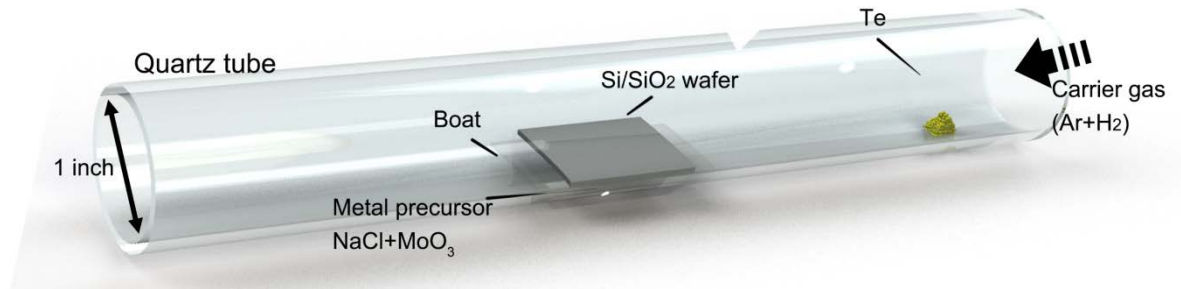
⁶Collaborative Innovation Center of Quantum Matter, Beijing 100871, China

⁷National Institute of Advanced Industrial Science and Technology (AIST), Tsukuba 305-8565, Japan

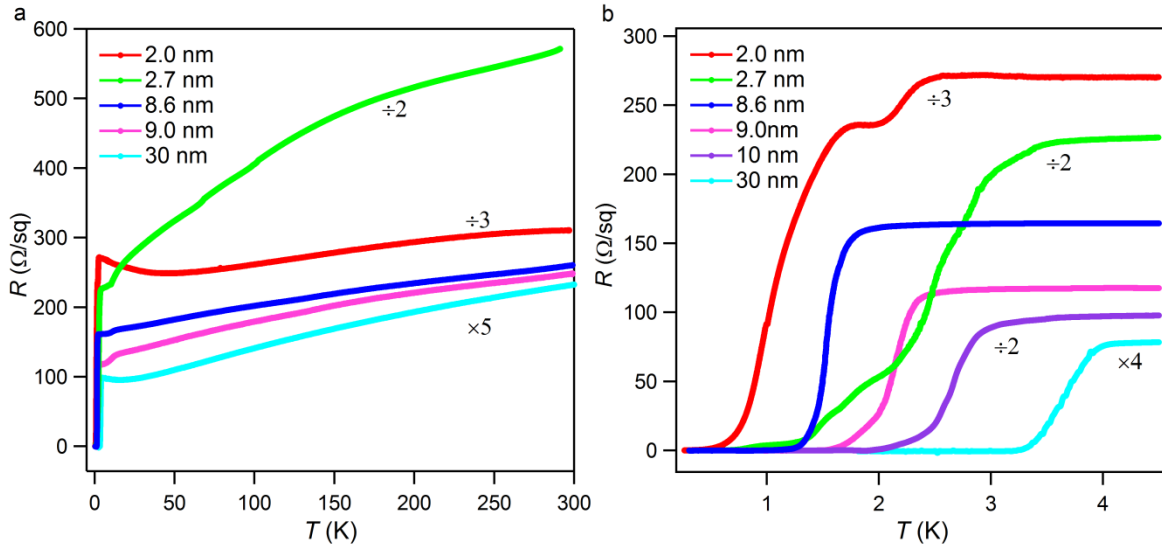
⁸Centre for Micro-/Nano-electronics (NOVITAS), School of Electrical & Electronic Engineering, Nanyang Technological University, 50 Nanyang Avenue, Singapore 639798, Singapore

⁹CINTRA CNRS/NTU/THALES, UMI 3288, Research Techno Plaza, 50 Nanyang Drive, Border X Block, Level 6, Singapore 637553, Singapore

† These authors contributed equally to this work. Correspondence and requests for materials should be addressed to J.L (email:lin.junhao@aist.go.jp), Z.L. (email: z.liu@ntu.edu.sg) and G.L (email:gtliu@iphy.ac.cn)



Supplementary Figure S1. The growth setup used for the controlled synthesis of few-layer MoTe_2 . In our experiment, the growth parameters were optimized to get better MoTe_2 films. The mixed compounds (MoO_3 : NaCl =5:1) are placed in the center of the tube. Si/SiO_2 substrate was placed on the alumina boat with the polished side faced down. Another alumina boat containing Te powder was put on the upstream side of quartz tube at a temperature of ~ 450 °C. Mixed gas of H_2/Ar with a flow rate of 15/80 sccm was used as the carrier gas. The furnace was ramped to 700 °C at a rate of 50 °C/min and held there for about 4 min to allow the growth of few-layer MoTe_2 crystals. After the reaction, the temperature was naturally cooled down to room temperature. All reagents were purchased from Alfa Aesar with purity exceeding 99%. The thickness can be controlled by the growth time from 2 to 15 min.



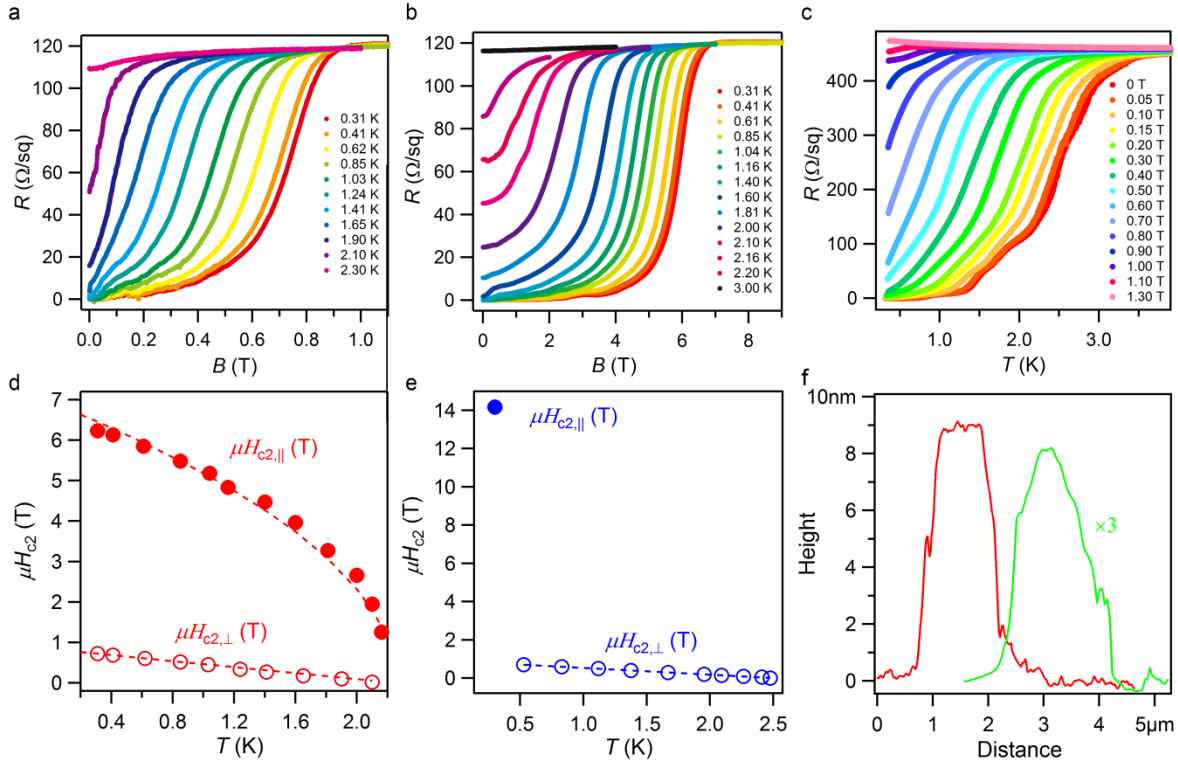
Supplementary Figure S2. Thickness dependence of the superconductivity in MoTe₂. **a**, Temperature dependence of sheet resistance of MoTe₂ with various thicknesses. For clarity, the data for 2-nm-thick and 2.7-nm-thick MoTe₂ were divided by 3 and 2, while the data was multiplied by 5 for 30-nm-thick MoTe₂, respectively. **b**, Temperature dependence of sheet resistance of MoTe₂ with various thicknesses in the range from 0.3 K to 5.5 K. For clarity, the data for 2-nm-thick, 2.7-nm-thick, and 10-nm-thick MoTe₂ were divided by 3, 2 and 2, while the data was multiplied by 4 for 30-nm-thick MoTe₂, respectively. Totally, a dozen of few-layer MoTe₂ samples were measured and all of them show metallic behavior at high temperatures before a superconducting transition emerging.

d	RRR	R_{5K} (Ω/sq)	r	$T_{c,r}$ (K)	ξ_{GL} (nm)	$\mu_0 H_{c2,\parallel}$ (T)	d_{sc} (nm)
2.0 nm	1.15	810.0	0	0.35	-	-	-
			0.5	1.12	-	-	-
			0.9	2.14	-	-	-
2.7 nm	2.51	454.6	0.05	1.31	25.40	10.67	2.69
			0.5	2.48	19.33	14.30	3.86
			0.9	3.12	17.55	15.30	4.04
3.0 nm	2.17	637.0	0.05	1.61	28.38	13.30	2.72
			0.5	2.32	19.29	19.69	2.80
			0.9	2.92	17.17	23.38	2.69
6.5 nm	0.76	488.2	0.05	1.15	18.79	5.80	8.99
			0.5	1.92	16.42	8.50	7.50
			0.9	2.57	13.97	10.10	7.60
8.6 nm	1.61	163.7	0.05	1.10	30.95	4.14	7.81
			0.5	1.54	20.79	5.38	9.15
			0.9	1.71	19.23	6.68	8.05
9.0 nm	2.10	118.5	0.05	1.50	30.45	3.88	8.75
			0.5	2.13	19.70	5.87	9.13
			0.9	2.32	18.83	6.40	8.83
10 nm	-	196.0	0	1.90		-	-
			0.5	2.66		-	-
			0.9	2.92		-	-
30 nm	2.36	19.70	0	3.16		-	-
			0.5	3.65		-	-
			0.9	3.91		-	-

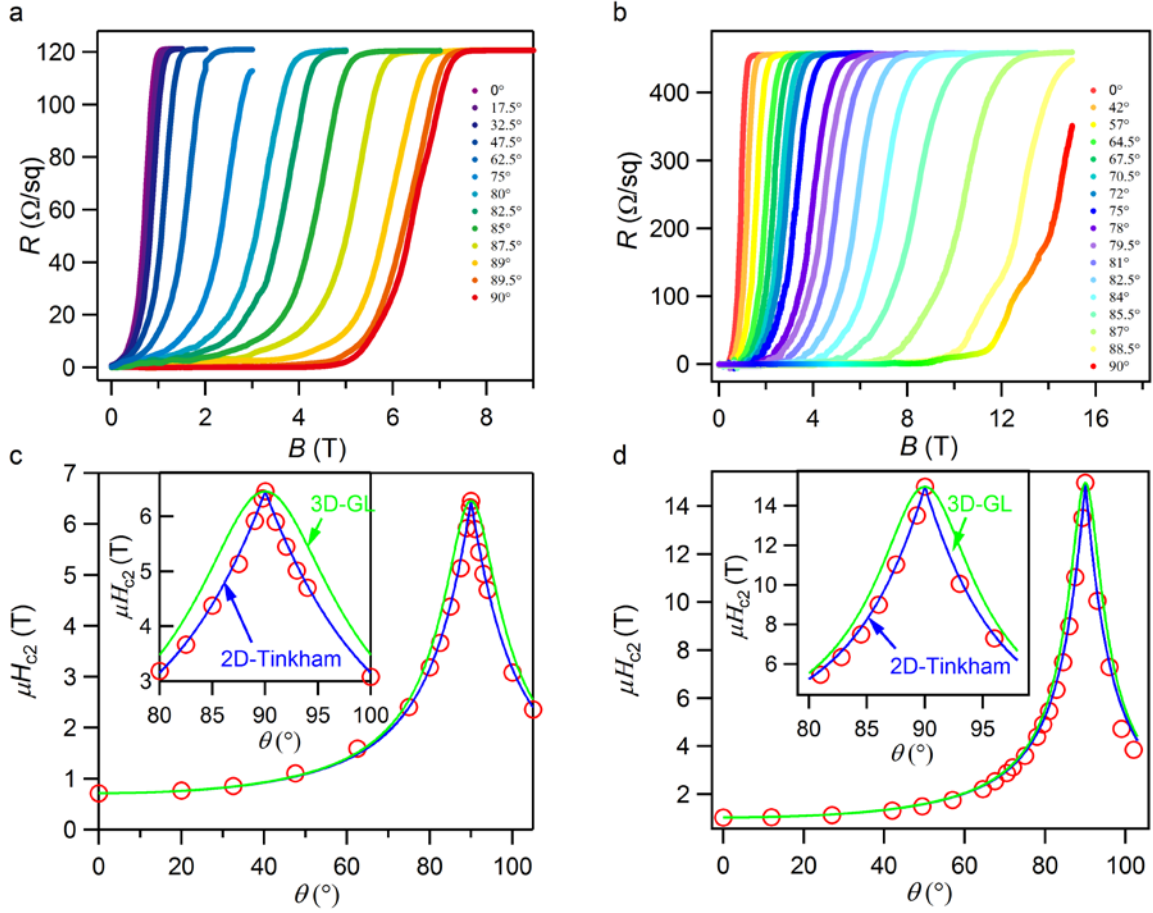
*RRR is defined by the ratio of the resistance at 300 K to the normal state resistance right above the superconducting transition, and $r = R/R_N = R/R_{5K}$. Values of $\mu_0 H_{c2,\perp}$ and $\mu_0 H_{c2,\parallel}$ corresponding to individual r were extracted from magnetoresistance traces measured at $T=0.3$ K, and the ξ_{GL} and d_{sc} were estimated from $H_{c2,\perp}(T) = \frac{\phi_0}{2\pi\xi_{GL}^2} \left(1 - \frac{T}{T_{c,0}}\right)$ and $H_{c2,\parallel}(T) = \frac{\phi_0\sqrt{12}}{2\pi\xi_{GL}d_{sc}} \sqrt{1 - \frac{T}{T_{c,0}}}$ with $T=0.3$ K, respectively. Beyond 15T the highest accessible magnetic field of our ^3He system, the $H_{c2,\parallel}$ values shown in red color were obtained from extrapolation of the experimental data.

Supplementary Table S1. Parameters of the measured MoTe_2 samples: Sample thickness (d), residual resistance ratio (RRR), sheet resistance at $T=5\text{K}$ (R_{5K}), and the set of parameters

corresponding to individual reduced sheet resistance (r): critical temperatures ($T_{c,r}$), perpendicular ($\mu_0 H_{c2,\perp}$) and in-plane ($\mu_0 H_{c2,\parallel}$) upper critical fields, zero-temperature superconducting coherence length (ξ_{GL}) and the superconducting thickness (d_{sc}).



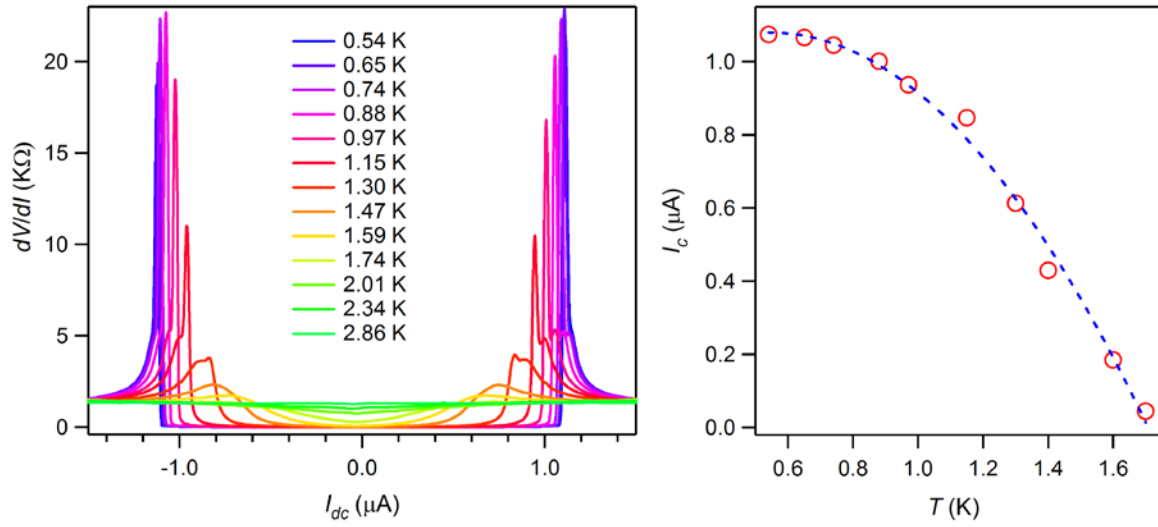
Supplementary Figure S3. Two-dimensional superconductivity of few-layer MoTe₂ crystals. Temperature dependence of superconducting resistive transition of the 9-nm-thick MoTe₂ crystal in perpendicular magnetic field (**a**) and in parallel magnetic field (**b**). **c**, Temperature dependence of superconducting resistive transition of the 2.7-nm-thick MoTe₂ crystal in perpendicular magnetic field. **d**, **e**, Temperature dependence of the upper critical field $\mu_0 H_{c2,\parallel}(T)$ and $\mu_0 H_{c2,\perp}(T)$, with magnetic field parallel and perpendicular to the crystal plane respectively, of the 9-nm-thick (**d**) and the 2.7-nm-thick (**e**) MoTe₂ crystals. Dashed curves correspond to fittings to the 2D Ginzburg-Landau theory. **f**, AFM height profiles of two typical few-layer MoTe₂ crystals.



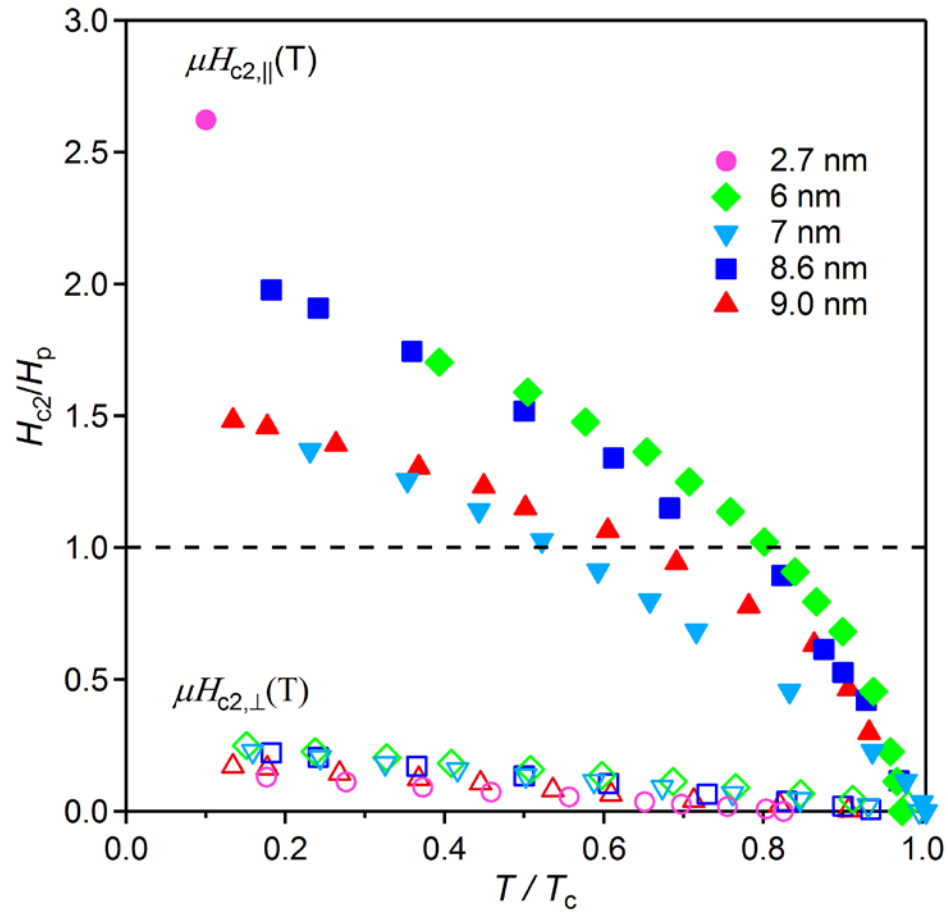
Supplementary Figure S4. Two-dimensional superconductivity of few-layer MoTe₂ crystals. **a**, **b**, Magnetic field dependence of the sheet resistance of a 9-nm-thick (**a**) and 2.7-nm-thick (**b**) MoTe₂ device at different tilted angles θ (the angle between a magnetic field and the normal of sample plane) at $T=0.3$ K. **c**, **d**, Angular dependence of the upper critical field $\mu_0 H_{c2}$ of a 9-nm-thick (**c**) and 2.7-nm-thick (**d**) MoTe₂ device. The solid lines represent the fitting with 2D

Tinkham formula $\left| \frac{H_{c2}(\theta) \cos \theta}{H_{c2,\perp}} \right| + \left(\frac{H_{c2}(\theta) \sin \theta}{H_{c2,\parallel}} \right)^2 = 1$ (blue line) and 3D anisotropic mass model

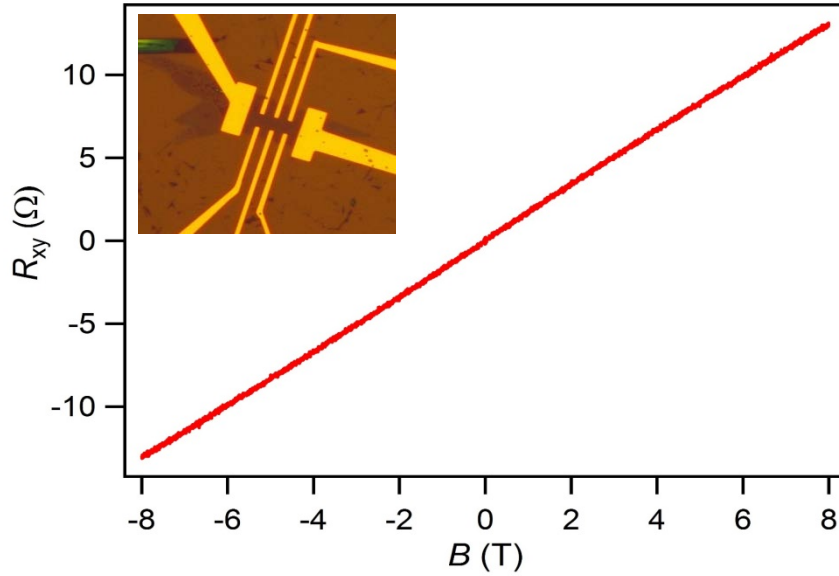
(3D-GL) $\left(\frac{H_{c2}(\theta) \cos \theta}{H_{c2,\perp}} \right)^2 + \left(\frac{H_{c2}(\theta) \sin \theta}{H_{c2,\parallel}} \right)^2 = 1$ (green line), respectively.



Supplementary Figure S5. a, Differential resistance of a 6.5-nm-thick MoTe₂ as a function of bias current at different fixed temperatures. The measurements were performed using a standard lock-in technique. The width of well-developed U-shape dV/dI curves narrows gradually with increasing temperature, and finally vanishes at ~ 2.0 K. **b**, Temperature dependence of the critical current I_c extracted from dV/dI curves. The dashed blue line is a guide to the eye.



Supplementary Figure S6. The phase diagram of $H_{c2} \sim T_c$ for few-layer MoTe₂. The out-of-plane upper critical fields $\mu_0 H_{c2,\perp}(T)$ and in-plane upper critical fields $\mu_0 H_{c2,\parallel}(T)$ are shown in solid and empty symbols, respectively. The dashed line denotes the Pauli limit $H_{c2} = H_p$.



Supplementary Figure S7. Hall resistance R_{xy} measured at 10 K for a 3.0-nm-thick MoTe₂ crystal. The inset shows the optical image of a typical Hall bar device. The data were collected in the normal state with the magnetic field perpendicular to the sample surface and with a current bias of 1 μ A. The carrier density and mean free path were estimated to be $2.52 \times 10^{14} \text{ cm}^{-2}$ and 10.3 nm by using the following procedure.

1) Estimation of carrier density n_s

By fitting the experimental data in Supplementary Figure S7, we can calculate the carrier density n_s by:

$$n_s = \frac{I/e}{dV_H/dB} = \frac{1/e}{dR_H/dB} = 2.52 \times 10^{14} \text{ cm}^{-2}$$

2) Estimation of sheet resistance R_s

The width w and length l for the measured sample can be determined by the optical image, $l=1.84 \mu\text{m}$, $w=1.75 \mu\text{m}$; The normal state resistance $R_N=669 \Omega$ was taken at $T=10.0 \text{ K}$. The sheet resistance R_s can be calculated by:

$$R_s = \frac{R_N w}{l} = 637 \Omega/\text{sq}$$

3) Estimation of mobility μ

According to the Drude model, the mobility μ can be calculated by:

$$\mu = \frac{1}{e R_s n_s} = 38.8 \text{ cm}^2/\text{Vs}$$

4) Estimation of the Fermi velocity v_F

In two-dimensional systems, the Fermi velocity v_F can be calculated by:

$$v_F = \frac{\hbar k_F}{m} = \frac{\hbar}{m} \sqrt{2\pi n_s} = 4.6 \times 10^5 \text{ m/s}$$

5) Estimation of the momentum scattering time τ_m

$$\tau_m = \frac{\mu m}{e} = 2.2 \times 10^{-14} \text{ s}$$

6) Estimation of the mean free path l_m

$$l_m = v_F \tau_m = \frac{\hbar k_F}{e} \mu = 10.3 \text{ nm}$$